Embedded droplet printing in yield-stress fluids

Arif Z. Nelson[a,b] (ORCID), Binu Kundukad[a,b,1], Wai Kuan Wong[c], Saif A. Khan[b,c,2], and Patrick S. Doyle[a,b,d,2] (ORCID)

[a]Biological Systems and Micromechanics, Singapore-MIT Alliance for Research and Technology, 138602 Singapore, Singapore; [b]Campus for Research Excellence and Technological Enterprise, 138602 Singapore, Singapore; [c]Department of Chemical and Biomolecular Engineering, National University of Singapore, 117585 Singapore, Singapore; and [d]Department of Chemical Engineering, Massachusetts Institute of Technology, Cambridge, MA 02139

Microfluidic tools and techniques for manipulating fluid droplets have become core to many scientific and technological fields. Despite the plethora of existing approaches to fluidic manipulation, non-Newtonian fluid phenomena are rarely taken advantage of. Here we introduce embedded droplet printing—a system and methods for the generation, trapping, and processing of fluid droplets within yield-stress fluids, materials that exhibit extreme shear thinning. This technique allows for the manipulation of droplets under conditions that are simply unattainable with conventional microfluidic methods, namely the elimination of exterior influences including convection and solid boundaries. Because of this, we believe embedded droplet printing approaches an ideal for the experimentation, processing, or observation of many samples in an "absolutely quiescent" state, while also removing some troublesome aspects of microfluidics including the use of surfactants and the complexity of device manufacturing. We characterize a model material system to understand the process of droplet generation inside yield-stress fluids and develop a nascent set of archetypal operations that can be performed with embedded droplet printing. With these principles and tools, we demonstrate the benefits and versatility of our method, applying it toward the diverse applications of pharmaceutical crystallization, microbatch chemical reactions, and biological assays.

yield-stress fluids | microfluidics | droplets | complex fluids | crystallization

Fluidic manipulation of micro- and milliscale droplets has become core to many fields and applications, including particle synthesis (1), chemistry (2, 3), and biology (4). There is an ever-expanding toolbox of methods for the generation, trapping, and processing of fluid droplets with volumes on the scale of 1 μL or below. However, persistent challenges and limitations remain such as the complexity of device manufacturing, a lack of flexibility with discrete channels and fixed geometries, and difficulty in selectively processing and extracting individual droplets. Efforts to address some of these challenges include the development of dynamic flow patterning (5), patterned substrates with "fluid walls" (6), and open microfluidic capillary systems (7, 8), yet inherent limitations are still present due to the primary reliance of these and other microfluidic methods on phenomena and fluids that are purely Newtonian. Non-Newtonian fluids have recently been exploited in microfluidics to control the flow focusing of particles and cells (9, 10), and rationally designed materials with dramatically non-Newtonian properties are of increasing interest for achieving novel performance that is simply unattainable with conventional materials. We demonstrate that by utilizing a class of non-Newtonian fluids known as "yield-stress fluids," we address many of the persistent challenges and inherent limitations of typical microfluidic technologies.

Yield-stress fluids are rheologically complex materials that reversibly transition from solid-like to fluid-like at a critical applied stress. When the applied stress exceeds the yield stress, these fluids will flow and deform readily; below the yield stress, suspended components are held in place. This complex behavior enables applications that range from familiar to fantastic, including hair gel, toothpaste, drug delivery (11–13), and 3D printing (14–16). There are numerous design routes one can take when formulating a yield-stress fluid, with many different

applicable chemistries and material structures (17). The engineering properties that we consider in this work include the yield-stress value, the postyield viscous effects [i.e., Herschel–Bulkley parameters (18)], optical properties, surface energy and wetting, and the ability to trigger mechanical changes in the yield-stress fluid.

Here we introduce embedded droplet printing—a system and methods for the generation, trapping, and processing of fluid droplets within yield-stress fluids; our methodology extends and improves on conventional microfluidics and draws inspiration from embedded 3D printing of continuous structures inside support materials (15, 19). By printing discrete droplets that are embedded within a bath of yield-stress fluid, we are not limited to fixed geometric boundaries, we can freely manipulate and process selected droplets for extended periods of time, and there is no complex device manufacturing. Furthermore, droplets embedded in yield-stress fluids are not affected by any solid boundaries or convective effects which are often inherent to other forms of microfluidics. This results in droplets with no mobility or risk of coalescence whatsoever, even without utilizing surfactants. Since our method combines many of the advantages of microfluidic technologies with predetermined spatial isolation and suppression or elimination of exterior influences like

---

Significance

Conventional microfluidic methods primarily rely on fluids that behave in simple ways, like water. Yield-stress fluids are materials that behave in a complex way, dramatically transitioning between solid-like and liquid-like behavior, depending on an applied stress. We introduce embedded droplet printing—a system for the generation and manipulation of fluid droplets within yield-stress fluids. Through the utilization of complex fluid behavior, we process droplets that are completely undisturbed by exterior fluid motion or solid boundaries and thus approach an ideal state for performing sensitive processes like pharmaceutical crystallization, which we demonstrate. The ability to controllably print and process droplets that are suspended in place is powerful and we believe has the potential to greatly impact many fluidic manipulation applications.

ENGINEERING

convection and solid boundaries, we believe this platform approaches an ideal for the experimentation, processing, or observation of many samples in an "absolutely quiescent" state.

In this work, we characterize the droplet generation process for a model pairing of yield-stress fluid and immiscible oil within a theoretically determined operating space. We show that non-dimensionalization using postyield viscous properties of the bath material yields a master curve for predicting droplet size. To demonstrate the benefits and versatility of our method, we develop a generic experimental toolbox for embedded droplet printing and apply these tools toward the diverse applications of pharmaceutical crystallization, microbatch chemical reactions, and biological assays.

Results and Discussion

Concept and Characterization of Embedded Droplet Printing. As depicted schematically in Fig. 1*A*, translating a nozzle that has been submerged in a bath of yield-stress fluid while simultaneously injecting an immiscible phase can produce suspended droplets. The bath yields due to the motion of the nozzle, and surface tension between the now-fluidized bath and injected fluid causes breakup of the injected fluid into spherical droplets. We couple a syringe pump to a motorized stage to print arrays of highly uniform droplets with a predictable volume in precise locations as shown in Fig. 1*B*. These droplets are embedded within the bath with no risk of coalescence or collapse without the use of surfactants and remain at their programmed locations for an essentially indefinite period of time—barring some triggered transformation of the bath material which we discuss later. This allows us to perform complex experimental processing of the droplets in a selective manner as exemplified by the addition of precise volumes of a secondary fluid shown in Fig. 1*C*.

The rheology of the yield-stress fluid bath determines the theoretical operating space for embedded droplet printing. Comparing

Fig. 1. (*A*) Schematic concept of embedded droplet printing. A submerged nozzle translating through a bath of yield-stress fluid while injecting an immiscible fluid can produce suspended droplets. The size, shape, and arrangement of these droplets can be highly regular and in three dimensions as shown in the experimental image in *B* with a 30-by-10-by-3 array of red-dyed oil droplets that are 1 mm in diameter, suspended in a water-based yield-stress fluid. The bath possesses rheological properties that suspend the droplets in place with no influence from exterior convective forces or solid surfaces. The bath provides barriers to contamination and allows for precise and complex experimental procedures to be performed as shown in the image in *C* with the injection of precise volumes of a red aqueous solution (up to 2 μL depicted) into previously printed blue aqueous droplets (initial volume ~4 μL) suspended in an oil-based yield-stress fluid.

the yield stress of the bath, σ_Y, to the stress exerted on the bath by a spherical droplet of diameter, d, due to buoyancy from a density difference, $\Delta\rho$ (20), we obtain

$$\frac{1}{2}\pi d^2 \sigma_Y > \frac{1}{6}\pi d^3 \Delta\rho g Y_{crit}, \qquad [1]$$

where g is the gravitational acceleration constant, and Y_{crit} is a dimensionless parameter defined as the ratio of the fluid's yield stress to the stress exerted on the fluid by the droplet when motion occurs due to a yielding transition (20, 21). Here we have rearranged the definition of Y_{crit} to describe our operating space of interest. One might naively expect Y_{crit} to be unity for yielding to occur, but due to the droplet needing only to yield a finite volume to move, theoretical studies have found a value of $Y_{crit} = 0.14$ for an idealized fluid (20, 22); experiments have shown Y_{crit} to be material specific, ranging between 0.05 and 0.6 (21, 23). Eq. **1** is the condition for a formed droplet to be statically suspended within the yield-stress fluid bath rather than sedimenting or floating due to buoyancy. Comparing the yield stress to the stress exerted due to surface tension γ, for a curved interface with diameter d, we obtain
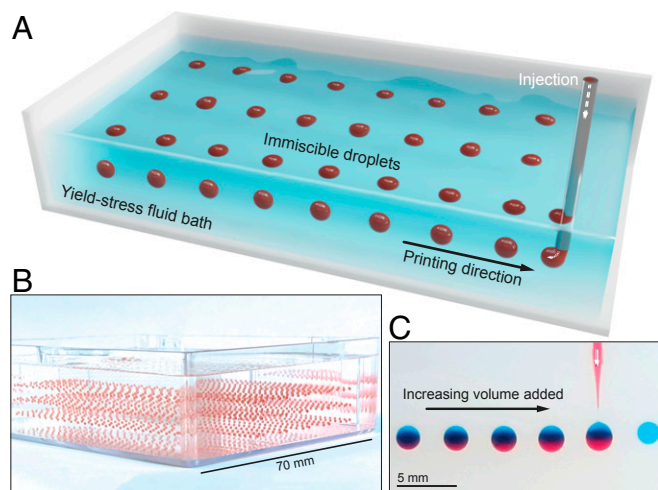
$$\sigma_Y < \frac{2\gamma}{d}. \qquad [2]$$

This inequality is the condition for whether droplet formation will occur at all. If the yield stress of the bath is too great, a continuous thread of the injected phase will form rather than discrete droplets; this regime has been taken advantage of for additive manufacturing with support baths of yield-stress fluids to produce vascular networks (24) and other 3D structures that would be otherwise difficult to manufacture (25, 26), but is not suitable for embedded droplet printing.
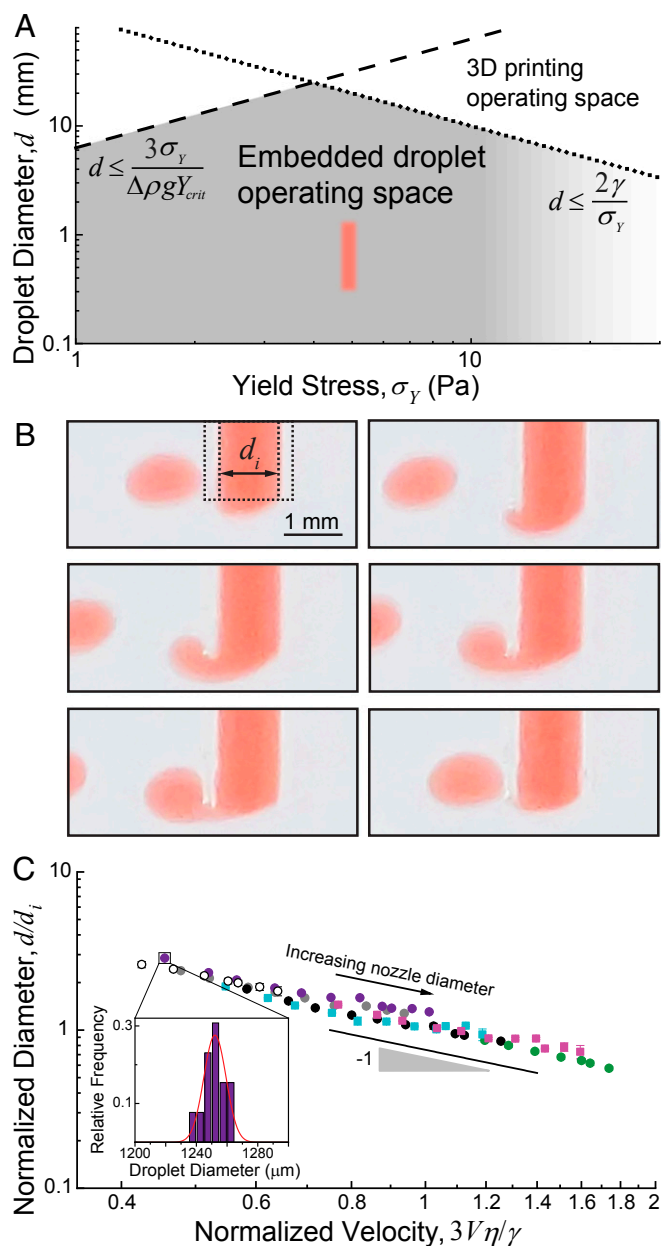
With these conditions, we determine an operating space for embedded droplet printing for a pairing of a model yield-stress fluid and an immiscible phase. We choose a light mineral oil as the immiscible phase and a well-known model yield-stress fluid, Carbopol, which is an aqueous jammed suspension of poly(acrylic acid) microgels (27). The rheology of Carbopol suspensions has been extensively characterized and they are generally considered "simple" yield-stress fluids (short thixotropic restructuring time) (28); conveniently, they are also optically transparent. Assuming the surface tension for our chosen system does not deviate significantly from that of water with mineral oil (29, 30) and using a reported value of 0.3 for Y_{crit} for Carbopol (21), Eqs. **1** and **2** result in the operating space depicted in Fig. 2*A*. There are likely other theoretical boundaries that one may draw; in particular, we have observed that relatively high-concentration Carbopol suspensions (higher yield stress and postyield viscosities) tend to result in inconsistent droplet production with significant wetting of the nozzle by the immiscible phase. We thus depict the right side of the operating space as having a soft boundary, but we leave a detailed exploration of this and any further nuances to future studies. We also limit our characterization of the droplet generation process to the orange-red region depicted in Fig. 2*A*.

The process of droplet generation is depicted in Fig. 2*B* (also Movie S1) for mineral oil (with red dye for visualization) being injected into an aqueous 0.1 wt% Carbopol yield-stress fluid. The dispersed phase grows at the nozzle exit and tends to fill the void left behind as the nozzle translates relative to the bath (toward the right in Fig. 2*B*). A neck forms at the edge of the nozzle outlet which further thins, and the droplet detaches from the nozzle. This process is similar to droplet breakoff in coflowing streams of Newtonian fluids, wherein droplets detach when the streamwise forces exceed the force due to interfacial tension (31).

There are many factors that one could choose to vary to characterize the droplet generation process. We perform a series

Fig. 2. (*A*) The operating space for embedded droplet printing is determined by capillary forces and buoyancy and is distinct from the operating space of embedded or direct-write 3D printing (15, 25). The equations shown are calculated for mineral oil in a water-based yield-stress fluid. The orange region depicts the range of experiments conducted in *C*. (*B*) Side-view image sequence (*Left* to *Right*, *Top* to *Bottom*) of droplet pinch-off with the relative translation of the nozzle toward the right side of the frame. A mineral oil with red dye is extruded into an aqueous yield-stress fluid, 0.1 wt% Carbopol, at a volumetric flow rate of 50 µL/min from a hydrophilically treated glass tube moving at a speed of 200 mm/min. Dotted lines are overlaid on the boundaries of the glass tube for clarity. The depicted sequence occurs over ∼800 ms. Droplets relax from an elongated into a spherical shape within several seconds of generation. (*C*) For our chosen model system, nondimensionalization yields a master curve in our operating range of interest. Nondimensionalized droplet diameter and velocity are shown for a set of mineral oil droplets printed in Carbopol from cylindrical nozzles made of steel (circle symbols) of nominal inner diameter 0.21 mm (open circles), 0.41 mm (gray circles), 0.44 mm (purple circles), 0.72 mm (black circles), and 1.5 mm (green circles) or hydrophilically treated glass (square symbols) of nominal inner diameter 0.67 mm (cyan squares) and 1 mm (magenta squares). All droplets were produced using a volumetric flow rate of 50 µL/min. Error bars smaller than the data points are neglected for clarity. *Inset* histogram depicts the relative frequency of droplet diameter for the indicated experimental point. The solid line is a Gaussian fit with $\sigma/\mu = 0.006$.

of experiments with our chosen model materials that systematically varies the velocity of the nozzle relative to the bath for different nozzle diameters and a fixed injection flow rate of 50 µL/min. We also vary nozzle materials between stainless steel and glass that has been plasma cleaned shortly before droplet generation to be hydrophilic and thus more readily wet by the bath phase. We obtain the droplet size as a function of velocity for droplets that range in diameter from ∼300 µm to 1.5 mm. The generated droplets are highly uniform in size, as depicted in Fig. 2 *C*, *Inset*; for a representative data point, the coefficient of variation, σ/μ, is 0.6%. Coefficient of variation information for all data points in Fig. 2*C* is available in *SI Appendix*, Fig. S3. The frequency of droplet pinch-off translates to a linear density of embedded droplets and a resulting spatial resolution. Across all experiments depicted in Fig. 2*C*, the maximum linear density we observe is 0.83 droplets per millimeter (see *SI Appendix*, Fig. S4 for a representative image). We control the spacing between rows and layers of printed droplets such that we achieve a maximum volumetric density of 66.4 droplets per milliliter of yield-stress fluid. The yielded region of the bath material due to a translating nozzle is a topic of interest for embedded 3D printing (15) and would also likely set the maximum volumetric density of embedded droplets, but this is outside the scope of our current work.

The analysis of the conventional, purely Newtonian case of droplet formation from coflowing streams balances the viscous Stokes' drag with the interfacial tension (31). This results in a normalized droplet size, d/d_i, where d_i is the inner diameter of the nozzle; and a capillary number, $3V\eta/\gamma$, where V is the velocity of the nozzle relative to the bath; and for us—unlike the conventional case—η is the non-Newtonian viscosity of the yield-stress fluid bath at a shear rate of V/d_o, where d_o is the outer diameter of the nozzle (see *SI Appendix*, Fig. S1 for bath rheology). Using these nondimensional variables that include the non-Newtonian viscosity, we obtain a master curve for this material system that has a power-law scaling of −1 as depicted in Fig. 2*C*. We verify for a subset of the nozzles that increasing the injection flow rate shifts the master curve slightly upward, but the overall scaling is preserved (see *SI Appendix*, Fig. S5 for detailed data). Thus, the variables derived for the Newtonian case can be simply modified to allow us to predict the size of resulting droplets for our model system. We have yet to explore what the effects of a wider range of different flow rates, nozzle geometries (e.g., tapered), or bath rheology and microstructure might be, but these and other effects are outside the scope of this current work.

Toolbox of Embedded Droplet Printing. The ability to controllably print and process droplets that are suspended in 3D space is powerful and we believe has the potential to greatly impact many fluidic manipulation applications. In the next sections, we demonstrate the versatility and benefits of embedded droplet printing in application, but first we must develop a toolbox of archetypal operations to work with beyond the single-phase injection depicted in Fig. 2*B*. These tools allow us to perform complex experimental processes for a wide variety of applications.

Fig. 3 *A* and *B* depicts two methods of mixing miscible components inside droplets—either injecting multiple components simultaneously via concentric nozzles or injecting a secondary component after the primary droplet printing process. After printed droplets have incubated for a desired amount of time, we may extract the contents of a selected droplet as depicted in Fig. 3*C* and continue to process or characterize them outside the bath environment if desired. For the aforementioned operations, appropriate wettability of the nozzles is crucial. For the primary droplet printing as depicted in Figs. 2*B* and 3*A*, we have observed that consistent results are obtained when the outermost nozzle surface is preferentially wet by the bath phase. For secondary

ENGINEERING
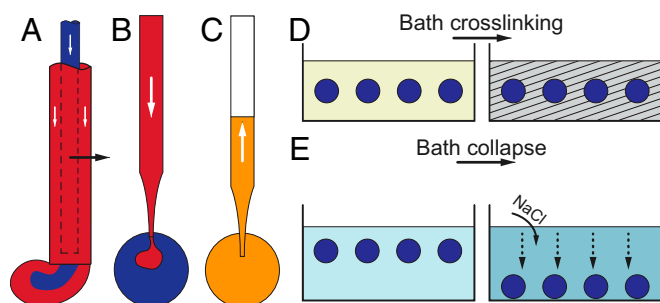
Fig. 3. The generic toolbox of embedded droplet printing allows for complex experimental scheduling to be performed and includes (*A*) point-of-injection mixing of miscible components via a concentric nozzle, (*B*) injection of additional fluid after an arbitrary time period after initial printing, and (*C*) extraction of fluid from incubated droplets. Postprinting, some bath materials may be (*D*) permanently cross-linked to facilitate handling and characterization, while others may allow for (*E*) removal of the yield-stress property from the bath material to enable droplet/particle recovery. For the 0.1 wt% Carbopol yield-stress fluid described in this work, the addition of a small amount of NaCl solution triggers a collapse of the microstructure.

injection or extraction (Fig. 3 *B* and *C*, respectively), the opposite is true: The nozzles must be preferentially wet by the droplet phase; otherwise droplets are simply pushed around and not pierced.

After droplet processing has been completed, we have explored two options for transforming the bath materials. Fig. 3*D* depicts a triggered solidification of the bath after printing. We achieve this with a bath whose composition includes a significant proportion of polydimethylsiloxane (PDMS) as well as a cross-linking agent. After droplet printing, this oil/PDMS-based bath permanently gels with gentle heating, trapping droplets inside. Droplets are fixed in place for extended periods of time, although droplet shrinking via evaporation through the PDMS can be observed after several days. Conceptually opposite to this, Fig. 3*E* depicts a triggered collapse of the bath microstructure (i.e., the bath loses its yield-stress property). This is achieved with the previously described Carbopol yield-stress fluid; the sizes of the polyacrylic acid microgels that compose this material are sensitive to pH as well as electrolyte concentration. Droplets are generated while the bath has a neutral pH (swollen microgels that are jammed). After printing, the electrolyte concentration is raised via the addition of sodium chloride, deswelling the microgels and allowing processed droplets to be recovered easily and en masse. The exploration and development of additional yield-stress fluids that exhibit useful triggered transformations is an area of future work that is of broad interest (17), and a wider range of formulations and triggering mechanisms would expand the number of experimental systems that embedded droplet printing would be suitable for.

In the remaining sections of this work we show how combinations of this set of relatively simple "tools" allow embedded droplet printing to be applied to a variety of important applications and establish why we believe this platform approaches an ideal for the experimentation, processing, or observation of many samples in an absolutely quiescent state.

Spherical Crystallization of Pharmaceutical Particles. In the production of pharmaceutical tablets, it is often necessary to have a flowable powder of crystallized active pharmaceutical ingredient (API) and excipient (32, 33). Granules of agglomerated crystals often have poor flowability in large part due to irregular shapes and wide size distributions, with many recent batch methods for crystallizing particles often still resulting in only what may be described as "approximately spherical" at best (34, 35). Microfluidic approaches to spherical crystallization offer significant improvements

in this regard (36), but crystals are often still marred by the deforming effects of viscous drag and interactions with other particles or solid surfaces, leading to noticeable deviations from sphericity (see *SI Appendix,* Fig. S6 for comparisons) or unintended nucleation. Furthermore, microfluidic approaches require the use of surfactants which are often an unwanted ingredient in a final powder product.

Embedded droplet printing allows for crystallization to occur under absolutely quiescent conditions. We utilize an antisolvent crystallization approach to produce uniform spherical particles inside our aqueous Carbopol yield-stress fluid as depicted schematically in Fig. 4*A*. We print droplets of ethyl acetate containing dissolved hydrophobic API and excipient. The droplets are spatially isolated with no risk of coalescence or collapse even though there are no surfactants present in either the droplet or the bath phase. The ethyl acetate is extracted into the aqueous bath since it is partially miscible in water, leaving behind a supersaturated API–excipient solution which crystallizes as shown in Fig. 4*B*. For our initial droplet diameter of 800 μm, the characteristic diffusion time (square of diameter divided by diffusivity) for ethyl acetate in water is ∼10 min (37). In these experiments, the volume of ethyl acetate extracted into the bath is less than 1% of the total bath volume, and thus we do not observe any change in the bath rheology due to dilution that would likely occur for significant or repeated injected volumes. Since the initial printed droplets are highly uniform and spherical due to Eq. **2** being satisfied, the crystallized particles share these characteristics. With embedded droplet printing, the extraction of ethyl acetate occurs purely diffusively, with no influence from viscous drag that may deform the droplet or from solid surfaces that would affect the nucleation process. Excepting some microgravity experimentation, embedded droplet printing is the only method that provides an environment in which droplets are spatially isolated from each other and solid surfaces and in which there are no exterior convective flows. Because of this, we believe that our technique approaches the ideal, completely undisturbed, conditions for terrestrial production of crystallized particles that are as spherical and uniform as possible, key targets in the manufacturing of pharmaceutical materials.

After crystallization has occurred, triggered collapse of the bath (Fig. 3*E*) enables convenient recovery of the sedimented particles as shown in Fig. 4*C* (also Movie S2). An example of the highly uniform spherical crystals we obtain is shown in Fig. 4*D* for a mixture of the hydrophobic API naproxen and excipient ethyl cellulose. For this unoptimized process, we produce ∼200 mg/h of particles in 300 mL of yield-stress fluid (i.e., 0.67 mg·h^{-1}·mL^{-1} yield-stress fluid). We are able to characterize the crystallinity of these particles via differential scanning calorimetry and X-ray powder diffraction as shown in Fig. 4 *E* and *F*, respectively; these indicate the presence of crystalline naproxen of form 1 (38).

Embedded Chemical Reaction Chambers. Microfluidic systems have gained great popularity for performing chemical reactions in part due to the ability to handle high throughputs of small and precise volumes of potentially expensive reagents (39, 40). With embedded droplet printing we maintain these advantages of microfluidic techniques over well-plate style batch processes, but by removing interactions with solid boundaries and external flow, we have considerably more freedom in arraying droplets. Embedded droplet printing eliminates reported challenges in droplet microfluidics such as droplet coalescence and collapse (41), reduces the risk of fouling in fixed geometries (42), and easily allows droplets to develop for extended timescales and be selectively addressed or directly sampled.

As a showcase for chemical synthesis using embedded droplet printing, we perform seed-mediated growth of silver nanoparticles as depicted schematically in Fig. 5*A*. By mixing aqueous seed solution and AgNO$_3$ in different proportions, nanoparticles grow to
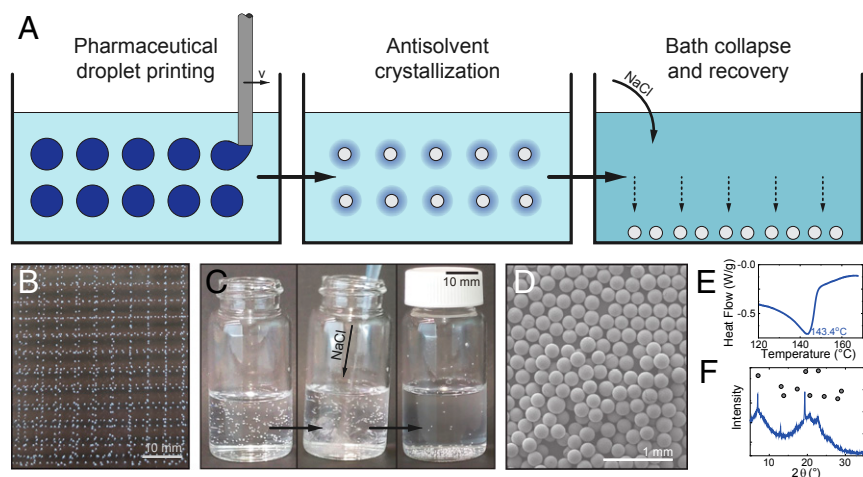
Fig. 4. Embedded droplet printing enables absolutely quiescent crystallization of spherical particles. (*A*) After printing of an appropriate pharmaceutical drug solution, antisolvent crystallization results in solid spherical particles that can be recovered after triggering the bath material structure to collapse. (*B*) Top–down view of droplets suspended in 0.1 wt% Carbopol that contain naproxen, a model hydrophobic API, and ethyl cellulose, an excipient. (*C*) Image sequence depicting a small volume (~1 mL) of 1 M NaCl being added to a 0.1 wt% Carbopol bath with initially suspended crystallized drug particles; within 60 s after being agitated, the Carbopol microstructure has collapsed, eliminating the yield-stress property and allowing for recovery and washing of the particles. (*D*) Field emission scanning electron microscopy image of naproxen and ethyl cellulose drug particles produced via the sequence described above. Compared to typical batch spherical crystallization techniques, embedded droplet printing produces highly uniform particles with no obvious common shape defects; see *SI Appendix*, Fig. S6 for details. (*E* and *F*) Differential scanning calorimetry thermogram (*E*) and X-ray powder diffraction plot (*F*) of the particles depicted in *D*, indicating the crystallinity of naproxen. The gray circles in *F* indicate the characteristic peaks for naproxen of form 1.

different sizes and shapes and produce different visible optical signatures (43). For this application, aqueous droplets are suspended within a silicone oil-based yield-stress fluid containing PDMS and a cross-linking agent. We make use of the point-of-injection mixing via concentric nozzles (Fig. 3*A*) to correlate input flow rates to the droplets being generated at a given time and position, as well as reduce the risk of fouling (compared to mixing in a T-junction fixture or similar process) (42, 44). As shown in Fig. 3 *B* and *C*, we are able to continuously or discretely change the proportions of reactants by controlling the flow rates of attached syringe pumps.

After droplets of known formulation are printed, the reactions may proceed for an extended period of time until they are ready to characterize (here, color change stops developing within 15 min). In many conventional microfluidic systems, procedures that require significant reaction times often have significant drawbacks. For example, flow and droplet generation might be paused as a reaction proceeds, limiting throughput and risking the merging of still-mobile droplets; droplets might also be circulated through very long or looping tubing, but this reportedly risks coalescence and collapse (41, 45). Alternatively, droplets could be deposited into a large reservoir or a trapping device that may be
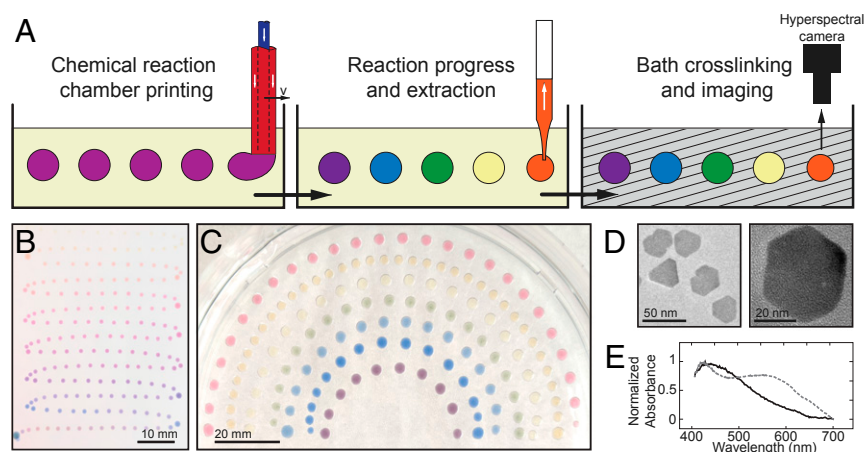
Fig. 5. Embedded droplet printing is a versatile platform for performing microbatch chemical reactions. (*A*) Precisely controlled quantities of multiple reagents may be simultaneously injected and allowed to react. After the reaction has progressed, fluid may be directly extracted, optically characterized, or both in sequence. As a model chemical process, we performed seed-mediated growth of silver nanoparticles. In the top–down photo shown in *B*, aqueous silver nanoparticle seed solution and AgNO₃ solution were mixed in continuously varying proportions as the droplets were printed into a bath composed of fumed silica, silicone oil, PDMS, and a cross-linker. Discrete jumps in the injected formulation are also possible as in the photo shown in *C*. Different proportions of seed to AgNO₃ solutions produce silver nanoparticles of varying sizes that give off different optical signatures. By exposing this bath material to low heating, the PDMS cross-links into a permanent gel, trapping droplets in place and allowing for easy handling and imaging. (*D* and *E*) Embedded droplets containing silver nanoparticles produced by the described method may be characterized by transmission electron microscopy as shown in (*D*) images of silver nanoparticles extracted from two different embedded droplets or by spectral imaging as shown in (*E*) absorbance spectra of two representative embedded droplets.

ENGINEERING

complex to manufacture; these techniques typically randomize the droplet placement inside sealed devices, making indexing and extraction difficult. Using embedded droplet printing, we do not have any of these limitations, and we believe time-lapse studies will be greatly facilitated.

With embedded droplet printing, we can directly extract products from droplets of interest (Fig. 3C) for characterization such as with transmission electron microscopy (TEM) as shown in Fig. 5D, verifying that nanoparticle shape and size vary for different droplet compositions; this kind of selective extraction remains challenging in conventional microfluidic systems. By transforming the yield-stress fluid into a permanent solid material, we facilitate handling and additional characterization of embedded droplets. As described in Fig. 3D, gentle heating triggers our bath material to cross-link, fixing the droplets in place. No change in color of the droplets was observed during this heating process. The bath material remains semitransparent after cross-linking and we optically characterize the droplets in situ via a hyperspectral camera. Fig. 5E shows representative absorbance spectra that we obtain. The spectra are peak shifted compared to a purely spherical silver nanoparticle case (46), indicating the presence of anisotropic nonspherical particles as expected and as seen in the TEM images. Without cross-linking of the bath material, this process would have been difficult; due to the low yield stress of the bath material, transportation of the entire bath is challenging without droplets shifting position and potentially merging.

Embedded Biological Assays. Similar to chemical applications, biological experiments are often extremely limited in terms of sample quantities and availability of expensive reagents, thus leading to increased usage of microfluidics for experiments like bioassays (4, 47). With embedded droplet printing, droplets containing biological samples are able to incubate for long periods of time but are continually directly addressable and recoverable; the droplets are stabilized without the use of molecular surfactants and are protected from exterior contaminants by the bath material. The lack of added surfactant molecules eliminates micelle formation as a mechanism for cross-droplet material transfer, an issue which has been reported to occur with droplet-based microfluidics systems (48). Additionally, compared to traditional droplet microfluidics assays containing microorganisms, the long-term stability of our droplets is not affected by mechanical agitation, wetting of the droplets with sidewalls, or the synthesis of new biomolecules by the microorganisms (4).

As depicted schematically in Fig. 6A, we culture droplets containing aqueous growth media and the model green fluorescent protein-expressing bacteria, *Pseudomonas aeruginosa*. This type of bacteria is an opportunist pathogen responsible for infections in patients under a variety of conditions. These droplets are printed inside the same oil-based yield-stress fluid described in the previous section but with no cross-linking agent added. The droplets are left to incubate at room temperature for 24 h, during which time the bacteria consolidate at the center of the droplet. We then inject known volumes of citric acid solution, a weak acid drug (49, 50), and a dead stain into each of the arrayed droplets (Fig. 3B) and obtain a range of final drug concentrations. After 2 additional hours of incubation, we image the droplets with a confocal microscope to determine whether the bacteria are alive (green fluorescence) or dead (red fluorescence) as shown in Fig. 6B.

As expected, at low citric acid concentrations, nearly the entire bacterial population is alive. The bath material is permeable to oxygen and thus the bacteria are able to survive as long as there are sufficient nutrients and low concentrations of waste within the growth media droplets. At a critical concentration above 2 mg/mL of citric acid, the bacteria rapidly die. As with many conventional microfluidic techniques, in general, embedded droplet printing would allow for faster drug screening compared to traditional batch methods. If desired, the droplet contents could be transferred onto an agar plate to detect the presence of any colony-forming units.

Although we do not demonstrate it here, one would also be able to easily extract fluid and samples from a given droplet (Fig.
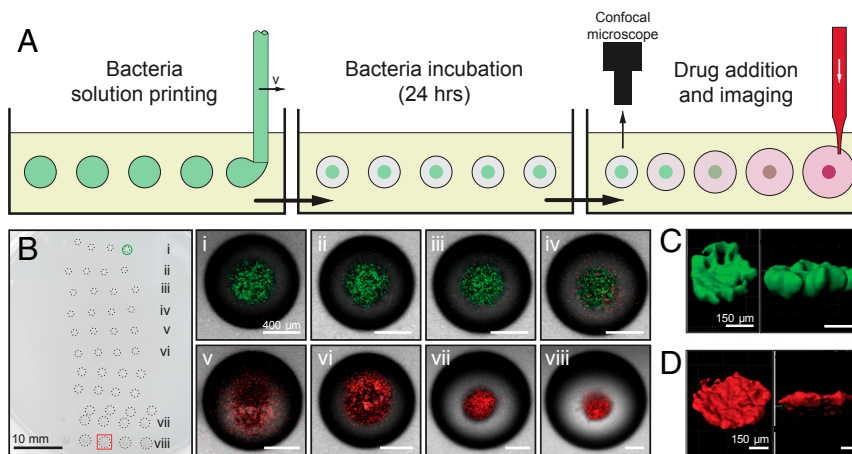
Fig. 6. Embedded droplet printing allows for small-volume bioassays with directly accessible droplets. (A) Solutions of bacteria and growth media are injected and allowed to incubate. After a prescribed amount of development time, a precise volume of a drug is injected into each droplet of interest which can then be characterized. We print droplets of *P. aeruginosa* and growth media that are able to survive for over 24 h embedded within a bath composed of fumed silica, silicone oil, and PDMS due to the permeability of the bath to oxygen. Twenty-four hours after printing, we inject varying volumes of a 10 mg/mL citric acid solution. After 2 additional hours, we characterize the droplets using confocal microscopy. Living bacteria give off a green fluorescent signal while dead bacteria give off a red fluorescent signal. (B) Top–down view of suspended droplets after injection of citric acid (dotted lines are overlaid on interfaces of characterized droplets for clarity). The roman numerals labeling each row correspond to the confocal images of a representative droplet from that row. The drug concentrations depicted are (*i*) 0 mg/mL, (*ii*) 0.5 mg/mL, (*iii*) 1 mg/mL, (*iv*) 2 mg/mL, (*v*) 3 mg/mL, (*vi*) 4 mg/mL, (*vii*) 8 mg/mL, and (*viii*) 9 mg/mL. (Scale bars in B, *i–viii*, 400 μm.) (C and D) Isometric and side views of Z-stack surface reconstructions of the bacteria colony for the green circled droplet in B are shown in C and those for the red square-outlined droplet in B are shown in D. Due to the lack of cross-linking of the bath to facilitate postincubation addition, the droplets in B shifted slightly from their original positions during handling and characterization. See *SI Appendix*, Figs. S7 and S8 for fluorescent images of each droplet in B.

3C) for further culturing outside the bath if desired or for proteomic analysis. By combining extraction with secondary injection (Fig. 3B), one could remove waste and supply new growth media for extended periods of culturing inside the bath. In embedded droplet printing, as long as the buoyant stress does not exceed the yield stress (Eq. **1**), the droplets act as chambers that would be bound in size only by the overall dimensions of the yield-stress fluid bath; this means that biological samples could potentially grow inside a droplet that continually scales up in size to accommodate them via the injection of additional fluid. A unique attribute of our platform is that we can reconfigure and merge two droplets at some selected time point by pushing them into contact using a nonwetting nozzle and then bridging them (Movies S3 and S4), which would not be possible with well-plate experiments. This feature could be exploited to simulate an infection in which one host grows for some time before encountering another species or multispecies studies to better understand the microbiome.

Summary and Conclusions

We introduced embedded droplet printing, a platform for the generation, trapping, and processing of suspended droplets. We characterized a model material system and obtained a master curve to enable the prediction of droplet size. We demonstrated how embedded droplet printing makes use of conventional microfluidic methods but extends their functionality through the use of yield-stress fluids, allowing for experimentation on and observation of droplets in an absolutely quiescent state using a toolbox of archetypal operations. We demonstrated how this completely undisturbed state appears to approach an ideal for the crystallization of small molecules. We demonstrated the flexibility and directly accessible nature of embedded droplet printing through microbatch chemical reactions and droplet-based biological assays. We propose that the unique functionality of embedded droplet printing can be put to even greater use as suggested throughout this paper. While we demonstrated that embedded droplet printing allows for a wide variety of applications, there are further inspirations from existing microfluidic technologies that could be adapted in future studies for even greater functionality; these include the generation of multiple-emulsion droplets and continuous-throughput production via an open-channel flow system. Future studies will be dedicated to optimizing the process to increase throughput, as well as exploring and refining the boundaries of the proposed operating space.

Materials and Methods

Yield-Stress Fluid Bath Preparation.
Materials. Carbopol 980 (cross-linked polyacrylic acid particles) was obtained from Lubrizol. Ultrapure water (18.2 MΩ) was obtained from a Sartorius H2OPRO-DI-T Arium Pro purifier. Sodium hydroxide (221465) and silicone oil (317667) were purchased from Sigma-Aldrich. Hydrophilic silica nanoparticles (AEROSIL 200) were obtained from Evonik Industries. PDMS and curing agent (Sylgard 184) were obtained from Dow Corning.
Water-based yield-stress fluid. Aqueous jammed suspensions of polymer microgels were prepared by mixing Carbopol 980 powder in ultrapure water at a concentration of 0.1 wt%. This solution was mixed for 30 min before being neutralized to pH 7 using a 1- M sodium hydroxide solution. This solution was placed in a vacuum chamber to remove air bubbles.
Oil-based yield-stress fluid. Silica nanoparticle oleogels similar to those described by Grosskopf et al. (15) were prepared by adding PDMS and then silicone oil to hydrophilic silica powder to achieve a final composition of 4 wt% silica, 48 wt% PDMS, 48 wt% silicone oil. This solution was first mixed vigorously by hand and then placed on an IKA Eurostar 40 digital stand mixer with a four-bladed propeller stirrer (R1342) to mix for 15 min at 2,000 rpm. If the bath was to be cross-linked, immediately prior to droplet printing, the yield-stress fluid and curing agent were mixed in a 10:1 ratio (wt/wt) and placed in a vacuum chamber to remove air bubbles. For consistent shear history and printing conditions, even if no cross-linker was to be added, immediately prior to droplet printing, this bath material would be vigorously mixed and the bubbles removed.

Motorized Platform System. For computer control of our droplet generation, we use the motorized platform of a 3Drag open-source 3D printer purchased from Open Electronics with an Arduino running Marlin firmware that accepts G-code commands through the freely available software Repetier. To the stationary frame of this platform, we mount nozzles that are either flat-tipped needles or surface-treated glass capillaries. Nozzle surfaces were modified to be preferentially wet by either the bath or the droplet phase, depending on the situation as discussed in *Toolbox of Embedded Droplet Printing*. For hydrophobic modification, nozzles were plasma cleaned and then treated with the commercial product Rain-X according to the manufacturer instructions. For hydrophilic modification, nozzles were plasma cleaned and submerged in ultrapure water for storage before printing. For secondary injection and extraction, prepulled glass micropipettes with a nominal tip diameter of 20 μm from FIVEphoton Biochemicals were used. Nozzles are connected via poly(tetrafluoroethylene) tubes (inner diameter 1 mm) purchased from Cole Parmer to 2.5-mL glass syringes (Hamilton GASTIGHT) purchased from Sigma-Aldrich mounted in Harvard Apparatus syringe pumps (PHD ULTRA 70-3007). We use custom-made 3D printed mounts to hold containers of yield-stress fluid in place on the motorized stage.

Characterization of Model System.
Materials. Light mineral oil (330779) was purchased from Sigma-Aldrich. For Figs. 1B and 2B and Movie S1 only, a commercial red food dye was added to the mineral oil for clarity. In all other cases, the mineral oil was used as received. Flat-tipped stainless steel needles were purchased from Taobao in nominal sizes of (inner diameter:outer diameter in millimeters) 0.21:0.42, 0.41:0.72, 0.44:0.8, 0.72:1.08, and 1.5:1.8 mm. Glass capillary tubes were purchased from VWR in nominal sizes of 0.67:1 and 1:1.5 mm and were plasma cleaned immediately prior to droplet printing. Stainless steel needles were not plasma cleaned. Sixty-millimeter diameter Petri dishes were purchased from Thermo Scientific. Carbopol solution (0.1 wt%) was prepared as described above.
Single-phase droplet printing and characterization. Nozzles were mounted to the stationary frame of the motorized platform described above and connected to a gas-tight glass syringe filled with mineral oil that was placed in a Harvard syringe pump. Petri dishes were filled with Carbopol solution to a thickness of ~1 cm and mounted on the motorized stage. The nozzle was positioned at a nominal height of 5 mm above the bottom of the dish. The platform was programmed to move in a serpentine pattern at progressively faster speeds starting at 100 mm/min and ending at 3,000 mm/min, with 2.5 mm between rows (G code available in ref. 51). Row spacing of 2.5 mm and layer spacing of 5 mm were used to calculate the volumetric density of droplets. Just after nozzle translation initiated, the mineral oil was injected at a volumetric flow rate of 50 or 100 μL/min (SI Appendix) via the syringe pump. Droplets were imaged on an inverted Olympus IX71 microscope with a 4× or 10× objective. Droplet size and linear density measurements were made using ImageJ. Dimensional drop size data and a representative image of maximum linear density are available in SI Appendix.
Rheological characterization of bath material. Rheological characterization of steady flow properties was performed on an AR-G2 combined motor/transducer rotational rheometer from TA Instruments, using parallel-plate geometry with a diameter of 40 mm and a Peltier temperature controller set to 25 °C. A range of shear rates was applied from high to low and the apparent steady stress was recorded and fitted to a Herschel–Bulkley model using Origin 2019 and used to calculate the corresponding viscosity as a function of the shear rate. These data are available in SI Appendix.

Spherical Crystallization of Pharmaceutical Particles.
Materials. Naproxen (N8280), ethyl cellulose (viscosity 10 cP 200689), and sodium chloride (S5886) were purchased from Sigma-Aldrich. Ethyl acetate (HiPerSolv CHROMANOFORM for HPLC, ≥99.8%) was purchased from VWR International, LLC, and used as received. Ultrapure water (18.2 MΩ at 25 °C) was obtained from a Sartorius H2OPRO-DI-T Arium Pro purifier. Cell strainers with a mesh size of 100 μm were purchased from Fisher Scientific. Carbopol solution (0.1 wt%) was prepared as detailed above.
Production of crystallized particles. The drug-loaded injected phase was prepared by dissolving 50 mg of naproxen and 20 mg of ethyl cellulose per milliliter of ethyl acetate. This solution was delivered at a volumetric flow rate of 50 μL/min through a flat-tipped needle of nominal inner diameter 0.44 mm and nominal outer diameter 0.8 mm, submerged in the Carbopol bath material contained by a rectangular plastic box. The motorized platform was programmed to move at a constant linear speed of 1,000 mm/min in a multilevel serpentine pattern (G code available in ref. 51). After suspended droplets were generated, the bath and droplets were left

undisturbed for at least 20 min (double the characteristic diffusion time estimated in the main text) for crystallization to proceed. To collapse the Carbopol material, a volume of 1 M NaCl solution approximately equal to 5% of the volume of the bath was added followed by agitation of the bath (Movie S2). Particles were collected on a cell strainer, rinsed three times with ultrapure water, and vacuum dried at room temperature for at least 12 h prior to structural and polymorphic characterization.

Characterization of pharmaceutical particles. All samples were prepared for scanning electron microscopy on conventional stubs with a silicon wafer surface and were coated with ∼10 nm of platinum by sputter coating. A field-emission scanning electron microscope (JEOL JSM-6700F) at 5 kV accelerating voltage was used to image the particles. Polymorphic characterization of particles was analyzed using differential scanning calorimetry (DSC) and powder X-ray diffraction (PXRD) to examine their crystallinity. An X-ray diffractometer (Bruker; D8 Advance) was operated at 40 kV, 30 mA, and at a scanning rate of 1.06°/min over a range of 2θ from 2.5–30°, using a Cu radiation wavelength of 1.54 Å. For DSC, a Mettler Toledo DSC 882 apparatus was used. Approximately 5 mg of sample was crimped in a sealed aluminum pan and heated at 5 °C/min in the range of −20 to 180 °C using an empty sealed pan as a reference.

Embedded Chemical Reaction Chambers.

Materials. Silver nitrate (99.9%) from Strem Chemicals and hydrazine hydrate (50 to 60%), sodium borohydride (98%), poly(vinyl alcohol) (molecular weight 67,000), and sodium citrate tribasic dihydrate (99%) from Sigma-Aldrich Co. Ltd. were used as received without any further purification. Ultrapure water (18.2 MΩ at 25 °C) was obtained from a Milli-Q purifier. Petri dishes were purchased from Thermo Scientific.

Synthesis of silver seed solution. A total of 2 mL of 1 mM silver nitrate solution and 2 mL of 1 wt% aqueous poly(vinyl alcohol) solution are pipetted into a 20-mL glass bottle with a magnetic stirrer. The solution is stirred at 1,400 rpm to mix the precursor solution. After that, 2 mL of 2.5 mM sodium borohydride solution is added rapidly into the glass bottle. The product is left to stir for 15 min.

Synthesis of silver nanoparticles. Aqueous growth solution consists of 2 mL of seed solution, 3 mL 100 mM sodium citrate solution, 5 mL of 1 wt% poly(vinyl alcohol) solution, and 5 mL of 40 mM hydrazine solution. A total of 10 mL of 1 mM silver nitrate solution is prepared as the precursor solution. These two solutions are filled into separate gas-tight Hamilton syringes. The solutions are delivered by using two syringe pumps (Harvard PHD ULTRA) into a coaxial glass capillary microfluidic device with the outermost surface (1.5 mm outer diameter) treated with Rain-X according to the manufacturer instructions to be hydrophobic and more readily wet by the bath material. The growth solution flows through the inner channel while the fluid in the outer channel is the precursor solution. Near the tip of the device, the two solutions meet and are printed as a single droplet in the oil-based yield-stress bath that contains cross-linking agent as described above. Before printing, the oil-based yield-stress bath was conditioned as described above in a Petri dish at a thickness of ∼1 cm. To produce silver nanoparticles of various sizes in each droplet, a ramp program is used, where the growth solution flow rate is decreased from 100 to 55 μL/min and the precursor solution flow rate is increased from 5 to 50 μL/min.

Characterization of silver nanoparticles. To prepare for TEM imaging, the silver nanoparticles solution in the printed droplet is extracted from the bath via a pipette and diluted with ultrapure water. A drop of this diluted sample is placed onto a 200-mesh copper grid, which is dried overnight and analyzed using TEM (JOEL 2010; accelerating voltage 200 K). In addition, the optical properties of these silver nanoparticles are identified via Resonon Hyperspectral Imaging Systems (Pika L with Backlight stage). Before characterization, the Petri dish containing the bath and droplets was placed on a hot plate at 35 °C for several hours to cross-link the bath. Droplets were characterized within 24 h to avoid any observed evaporation through the now-porous PDMS material. With this hyperspectral system, the intensity of the light passing through each silver nanoparticle-containing droplet is recorded and used to compute the absorbance of the silver nanoparticle solution. Droplets of the same size containing only ultrapure water were used to obtain a reference absorbance.

Embedded Biological Assays.

Biofilm formation in microarrays. P. aeruginosa mucA strains, which were fluorescently tagged with green fluorescent protein (eGFP), were used to make the microprinted droplet arrays of biofilms. Overnight cultures of P. aeruginosa strains were grown in Luria–Bertani broth (5 g/L NaCl, 5 g/L yeast extract, 10 g/L tryptone) at 37 °C under shaking conditions (200 rpm). The overnight P. aeruginosa culture was diluted to an optical density at 600 nm (OD_{600}) of 0.4, and 1 mL of the culture was taken in a glass Hamilton syringe and printed into the oil-based yield-stress bath at a volumetric flow rate of 50 μL/min via a syringe pump (Harvard PHD ULTRA). The motorized platform was programmed to move at a constant linear speed of 500 mm/min in a serpentine pattern (G code available in ref. 51). The arrayed microdroplets of bacteria culture were then allowed to grow for 24 h to form blobs of biofilm.

Treatment, staining, and imaging. Citric acid (Sigma-Aldrich) at a concentration of 10 mg/mL prepared using LB medium was added to each droplet in varying volumes via a hydrophilically modified glass capillary connected to a syringe pump so that the final concentration in each droplet ranging from 0 to 9 mg/mL propidium iodide (PI) (Sigma-Aldrich) was added to citric acid to a final concentration of 60 μM to visualize the dead bacteria in biofilms. The citric acid–PI mixture was added to the microarrays and incubated for 2 h to allow for the action of citric acid on the bacteria and staining of the dead cells by PI.

The droplets were then imaged using a FluoView 1000 confocal microscope (Olympus) with a 4× objective. Three image channels, GFP 488, Alexa 594, and bright field, were acquired from each droplet. The 3D image stacks of the representative droplets were also acquired to visualize the biofilm structure within the droplets before and after treatment with the citric acid.

1. A. R. Abate *et al.*, Synthesis of monodisperse microparticles from non-Newtonian polymer solutions with microfluidic devices. *Adv. Mater.* **23**, 1757–1760 (2011).
2. A. J. DeMello, Control and detection of chemical reactions in microfluidic systems. *Nature* **442**, 394–402 (2006).
3. S. Mashaghi, A. Abbaspourrad, D. A. Weitz, A. M. van Oijen, Droplet microfluidics: A tool for biology, chemistry and nanotechnology. *TrAC Trends Analyt. Chem.* **82**, 118–125 (2016).
4. T. S. Kaminski, O. Scheler, P. Garstecki, Droplet microfluidics for microbiology: Techniques, applications and challenges. *Lab Chip* **16**, 2168–2187 (2016).
5. F. Paratore, V. Bacheva, G. V. Kaigala, M. Bercovici, Dynamic microscale flow patterning using electrical modulation of zeta potential. *Proc. Natl. Acad. Sci. U.S.A.* **116**, 10258–10263 (2019).
6. E. J. Walsh *et al.*, Microfluidics with fluid walls. *Nat. Commun.* **8**, 816 (2017).
7. B. P. Casavant *et al.*, Suspended microfluidics. *Proc. Natl. Acad. Sci. U.S.A.* **110**, 10111–10116 (2013).
8. E. Berthier, A. M. Dostie, U. N. Lee, J. Berthier, A. B. Theberge, Open microfluidic capillary systems. *Anal. Chem.* **91**, 8739–8750 (2019).
9. B. Kim *et al.*, Normal stress difference-driven particle focusing in nanoparticle colloidal dispersion. *Sci. Adv.* **5**, v4819 (2019).
10. E. J. Lim *et al.*, Inertio-elastic focusing of bioparticles in microchannels at high throughput. *Nat. Commun.* **5**, 4120 (2014).
11. C. H. Lee, V. Moturi, Y. Lee, Thixotropic property in pharmaceutical formulations. *J. Control. Release* **136**, 88–98 (2009).
12. E. A. Appel *et al.*, Self-assembled hydrogels utilizing polymer-nanoparticle interactions. *Nat. Commun.* **6**, 6295 (2015).
13. J. E. Mealy *et al.*, Injectable granular hydrogels with multifunctional properties for biomedical applications. *Adv. Mater.* **30**, e1705912 (2018).
14. J. A. Lewis, Direct-write assembly of ceramics from colloidal inks. *Curr. Opin. Solid State Mater. Sci.* **6**, 245–250 (2002).
15. A. K. Grosskopf *et al.*, Viscoplastic matrix materials for embedded 3D printing. *ACS Appl. Mater. Interfaces* **10**, 23353–23361 (2018).
16. B. M. Rauzan, A. Z. Nelson, S. E. Lehman, R. H. Ewoldt, R. G. Nuzzo, Particle-free emulsions for 3D printing elastomers. *Adv. Funct. Mater.* **28**, 1–12 (2018).
17. A. Z. Nelson *et al.*, Designing and transforming yield-stress fluids. *Curr. Opin. Solid State Mater. Sci.* **23**, 100758 (2019).
18. A. Z. Nelson, R. H. Ewoldt, Design of yield-stress fluids: A rheology-to-structure inverse problem. *Soft Matter* **13**, 7578–7594 (2017).
19. J. T. Muth *et al.*, Embedded 3D printing of strain sensors within highly stretchable elastomers. *Adv. Mater.* **26**, 6307–6312 (2014).

20. A. N. Beris, J. A. Tsamopoulos, R. C. Armstrong, R. A. Brown, Creeping motion of a sphere through a Bingham plastic. *J. Fluid Mech.* **158**, 219–244 (1985).
21. H. Emady, M. Caggioni, P. Spicer, Colloidal microstructure effects on particle sedimentation in yield stress fluids. *J. Rheol.* **57**, 1761–1772 (2013).
22. M. Beaulne, E. Mitsoulis, Creeping motion of a sphere in tubes filled with Herschel–Bulkley fluids. *J. Non-Newton. Fluid Mech.* **72**, 55–71 (1997).
23. R. P. Chhabra, *Bubbles, Drops, and Particles in Non-Newtonian Fluids* (CRC Press, 2006).
24. W. Wu, A. DeConinck, J. A. Lewis, Omnidirectional printing of 3D microvascular networks. *Adv. Mater.* **23**, H178–H183 (2011).
25. C. S. O'Bryan *et al.*, Three-dimensional printing with sacrificial materials for soft matter manufacturing. *MRS Bull.* **42**, 571–577 (2017).
26. C. S. O'Bryan *et al.*, Self-assembled micro-organogels for 3D printing silicone structures. *Sci. Adv.* **3**, e1602800 (2017).
27. J. M. Piau, Carbopol gels: Elastoviscoplastic and slippery glasses made of individual swollen sponges. Meso- and macroscopic properties, constitutive equations and scaling laws. *J. Non-Newton. Fluid Mech.* **144**, 1–29 (2007).
28. D. Bonn, M. M. Denn, Yield stress fluids slowly yield to analysis. *Science* **324**, 1401–1402 (2009).
29. L. Jørgensen, M. Le Merrer, H. Delanoë-Ayari, C. Barentin, Yield stress and elasticity influence on surface tension measurements. *Soft Matter* **11**, 5111–5121 (2015).
30. C. A. Stan, S. K. Y. Tang, G. M. Whitesides, Independent control of drop size and velocity in microfluidic flow-focusing generators using variable temperature and flow rate. *Anal. Chem.* **81**, 2399–2402 (2009).
31. P. B. Umbanhowar, V. Prasad, D. A. Weitz, Monodisperse emulsion generation via drop break off in a coflowing stream. *Langmuir* **16**, 347–351 (2000).
32. H. Leuenberger, New trends in the production of pharmaceutical granules: Batch versus continuous processing. *Eur. J. Pharm. Biopharm.* **52**, 289–296 (2001).
33. F. J. Muzzio, T. Shinbrot, B. J. Glasser, Powder technology in the pharmaceutical industry: The need to catch up fast. *Powder Technol.* **124**, 1–7 (2002).
34. H. Chen, A. Aburub, C. C. Sun, Direct compression tablet containing 99% active ingredient-A tale of spherical crystallization. *J. Pharm. Sci.* **108**, 1396–1400 (2019).
35. B. Ahmed *et al.*, Engineering of acetaminophen particle attributes using a wet milling crystallisation platform. *Int. J. Pharm.* **554**, 201–211 (2019).
36. E. W. Q. Yeap, A. J. Acevedo, S. A. Khan, Microfluidic extractive crystallization for spherical drug/drug-excipient microparticle production. *Org. Process Res. Dev.* **23**, 375–381 (2019).
37. K. A. Reddy, L. K. Doraiswamy, Estimating liquid diffusivity. *Ind. Eng. Chem. Fundam.* **6**, 77–79 (1967).
38. J. S. Song, Y. T. Sohn, Crystal forms of naproxen. *Arch. Pharm. Res.* **34**, 87–90 (2011).
39. K. F. Jensen, Flow chemistry-Microreaction technology comes of age. *AIChE J.* **63**, 858–869 (2017).
40. T. S. Kaminski, P. Garstecki, Controlled droplet microfluidic systems for multistep chemical and biological assays. *Chem. Soc. Rev.* **46**, 6210–6226 (2017).
41. L. Mazutis, "Microfluidic system and methods for highly selective droplet fusion." US Patent 9446360B2 (2010).
42. R. Mukhopadhyay, When microfluidic devices go bad. *Anal. Chem.* **77**, 429 A–432 A (2005).
43. I. Pastoriza-Santos, L. M. Liz-Marzán, Colloidal silver nanoplates. State of the art and future challenges. *J. Mater. Chem.* **18**, 1724–1737 (2008).
44. E. Dressaire, A. Sauret, Clogging of microfluidic systems. *Soft Matter* **13**, 37–48 (2016).
45. S. Zhang *et al.*, Microfluidic platform for optimization of crystallization conditions. *J. Cryst. Growth* **472**, 18–28 (2017).
46. Q. Zhang, N. Li, J. Goebl, Z. Lu, Y. Yin, A systematic study of the synthesis of silver nanoplates: Is citrate a "magic" reagent? *J. Am. Chem. Soc.* **133**, 18931–18939 (2011).
47. G. Amselem, C. Guermonprez, B. Drogue, S. Michelin, C. N. Baroud, Universal microfluidic platform for bioassays in anchored droplets. *Lab Chip* **16**, 4200–4211 (2016).
48. P. Gruner *et al.*, Controlling molecular transport in minimal emulsions. *Nat. Commun.* **7**, 10392 (2016).
49. B. Kundukad *et al.*, Mechanistic action of weak acid drugs on biofilms. *Sci. Rep.* **7**, 4783 (2017).
50. B. Kundukad *et al.*, Weak acids as an alternative anti-microbial therapy. *Biofilm* **2**, 100019 (2020).
51. A. Z. Nelson, Embedded-Droplet-Printing-Gcode-February-2020. Github. https://github.com/arifnelson/Embedded-Droplet-Printing-Gcode-February-2020. Deposited 20 February 2020.